

# Polar stratospheric nitric acid depletion surveyed from a decadal dataset of IASI total columns

Gaetane Ronsmans<sup>1,a</sup>, Catherine Wespes<sup>1,a,\*</sup>, Lieven Clarisse<sup>1</sup>, Susan Solomon<sup>2</sup>, Daniel Hurtmans<sup>1</sup>, Cathy Clerbaux<sup>1,3</sup>, and Pierre-François Coheur<sup>1</sup>

<sup>1</sup>Université libre de Bruxelles (ULB), Spectroscopy, Quantum Chemistry and Atmospheric Remote Sensing (SQUARES), Brussels, Belgium

<sup>2</sup>Department of Earth, Atmospheric and Planetary Sciences, Massachusetts Institute of Technology, Cambridge, Massachusetts, USA

<sup>3</sup>LATMOS/IPSL, Sorbonne Université, UVSQ, CNRS, Paris, France

\* Corresponding author: Catherine Wespes (catherine.wespes@ulb.be)

<sup>a</sup> Co-first authors

## Abstract

In this paper, we exploit the first 10-year data-record (2008-2017) of nitric acid (HNO<sub>3</sub>) total columns measured by the IASI-A/Metop infrared sounder, characterized by an exceptional daily sampling and a good vertical sensitivity in the lower-to-mid stratosphere (around 50 hPa), to monitor the relationship between the temperature decrease and the observed HNO<sub>3</sub> loss that occurs each year in the Antarctic stratosphere during the polar night. Since the HNO<sub>3</sub> depletion results from the formation of polar stratospheric clouds (PSCs) which trigger the development of the ozone (O<sub>3</sub>) hole, its continuous monitoring is of high importance. We verify here, from the 10-year time evolution of HNO<sub>3</sub> together with temperature (taken from reanalysis at 50 hPa), the recurrence of specific regimes in the annual cycle of IASI HNO<sub>3</sub> and identify, for each year, the day and the 50 hPa temperature ("drop temperature") corresponding to the onset of strong HNO<sub>3</sub> depletion in the Antarctic winter. Although the measured HNO<sub>3</sub> total column does not allow the uptake of HNO<sub>3</sub> by different types of PSC particles along the vertical profile to be differentiated, an average drop temperature of  $194.2 \pm 3.8$  K, close to the nitric acid trihydrate (NAT) existence threshold ( $\sim 195$  K at 50 hPa), is found in the region of potential vorticity lower than  $-10 \times 10^{-5}$  K.m<sup>2</sup>.kg<sup>-1</sup>.s<sup>-1</sup> (similar to the 70° – 90° S Eqlat region during winter). The spatial distribution and inter-annual variability of the drop temperature are investigated and discussed. This paper highlights the capability of the IASI sounder to monitor the evolution of polar stratospheric HNO<sub>3</sub>, a key player in the processes involved in the depletion of stratospheric O<sub>3</sub>.

## 1 Introduction

The cold and isolated air masses found within the polar vortex during winter are associated with a strong denitrification of the stratosphere due to the formation of PSCs (composed of HNO<sub>3</sub>, sulphuric acid (H<sub>2</sub>SO<sub>4</sub>) and water ice (H<sub>2</sub>O)) (e.g. Peter, 1997; Voigt et al., 2000; von König, 2002; Schreiner et al., 2003; Peter and Groö, 2012). These clouds strongly affect the polar chemistry by (1) acting as surfaces for the heterogeneous activation of chlorine and bromine compounds, in turn leading to enhanced O<sub>3</sub> destruction (e.g. Solomon, 1999; Wang and Michelangeli, 2006; Harris et al., 2010; Wegner et al., 2012) and by (2) removing gas-phase HNO<sub>3</sub> temporarily or permanently through uptake by PSCs and sedimentation of large PSC particles to lower altitudes. The denitrification of the polar stratosphere during winter delays the reformation of ClONO<sub>2</sub>, a chlorine reservoir, and, hence, intensifies the O<sub>3</sub> hole (e.g. Solomon, 1999; Harris et al., 2010; Tritscher et al., 2021). The heterogeneous reaction rates on PSC surfaces and the uptake of HNO<sub>3</sub> strongly depend on the temperature and on the PSC particles type. The

49 PSCs are classified into three different types based on their composition and optical properties: type Ia  
50 solid nitric acid trihydrate - NAT ( $\text{HNO}_3 \cdot (\text{H}_2\text{O})_3$ ), type Ib liquid supercooled ternary solution - STS  
51 ( $\text{HNO}_3/\text{H}_2\text{SO}_4/\text{H}_2\text{O}$  with variable composition) and type II, crystalline water-ice particles (likely  
52 composed of a combination of different chemical phases) (e.g. Toon et al., 1986; Koop et al., 2000;  
53 Voigt et al., 2000; Lowe and MacKenzie, 2008). In the stratosphere, they mostly consist of mixtures of  
54 liquid/solid STS/NAT particles in varying number densities, with  $\text{HNO}_3$  being the major constituent of  
55 these particles. The large-size NAT particles of low number density are the principal cause of  
56 sedimentation (Lambert et al., 2012; Pitts et al., 2013; Molleker et al., 2014; Lambert et al., 2016). The  
57 formation temperature of STS ( $T_{STS}$ ) and the thermodynamic equilibrium temperatures of NAT ( $T_{NAT}$ )  
58 and ice ( $T_{ice}$ ) have been determined, respectively, as:  $\sim 192$  K (Carslaw et al., 1995),  $\sim 195.7$  K (Hanson  
59 and Mauersberger, 1988) and  $\sim 188$  K (Murphy and Koop, 2005) for typical 50 hPa atmospheric  
60 conditions (5 ppmv  $\text{H}_2\text{O}$  and 10 ppbv  $\text{HNO}_3$ ). While the NAT nucleation was thought to require pre-  
61 existing ice nuclei, hence, temperatures below  $T_{ice}$  (e.g. Zondlo et al., 2000; Voigt et al., 2003), recent  
62 observational and modelling studies have shown that  $\text{HNO}_3$  starts to condense in early PSC season in  
63 liquid NAT mixtures well above  $T_{ice}$  ( $\sim 4$  K below  $T_{NAT}$ , close to  $T_{STS}$ ) even after a very short temperature  
64 threshold exposure (TTE) to these temperatures but also slightly below  $T_{NAT}$  after a long TTE, whereas  
65 the NAT existence persists up to  $T_{NAT}$  (Pitts et al., 2013; Hoyle et al., 2013; Lambert et al., 2016; Pitts  
66 et al., 2018). It has been recently proposed that the higher temperature condensation results from  
67 heterogeneous nucleation of NAT on meteoritic dust in liquid aerosol (Voigt et al., 2005; Hoyle et al.,  
68 2013; Grooß et al., 2014; James et al., 2018; Tritscher et al., 2021). Further cooling below  $T_{STS}$  and  $T_{ice}$   
69 leads to nucleation of liquid STS, of solid NAT onto ice and of ice particles mainly from STS (type II  
70 PSCs) (Lowe and MacKenzie, 2008). The formation of NAT and ice has also been shown to be triggered  
71 by stratospheric mountain-waves (Carslaw et al., 1998; Hoffmann et al., 2017). Although the formation  
72 mechanisms and composition of STS droplets in stratospheric conditions are well described (Toon et al.,  
73 1986; Carslaw et al., 1995; Lowe and MacKenzie, 2008), the NAT and ice nucleation processes still  
74 require further investigation (Tritscher et al., 2021). This could be important as the chemistry-climate  
75 models (CCMs) generally oversimplify the heterogeneous nucleation schemes for PSC formation (Zhu  
76 et al., 2015; Spang et al., 2018; Snels et al., 2019), preventing an accurate estimation of  $\text{O}_3$  levels.

77  
78 Several satellite instruments have measured stratospheric  $\text{HNO}_3$  over decades (e.g. MLS/UARS (Santee  
79 et al., 1999), MLS/Aura (Santee et al., 2007), MIPAS/ENVISAT (Piccolo and Dudhia, 2007), ACE-  
80 FTS/SCISAT (Sheese et al., 2017) and SMR/Odin (Urban et al., 2009)). Spaceborne instruments such  
81 as the CALIOP/CALIPSO lidar and MIPAS/Envisat measuring in the infrared are capable of detecting  
82 and classifying PSC types, allowing their formation mechanisms to be investigated (Lambert et al., 2016;  
83 Pitts et al., 2018; Spang et al., 2018, Tritscher et al., 2021 and references therein); these satellite data  
84 complement in situ measurements (Voigt et al., 2005) and ground-based lidar (Snels et al., 2019). From  
85 these available observational datasets, the  $\text{HNO}_3$  depletion has been linked to PSC formation and  
86 detected below the  $T_{NAT}$  threshold (Santee et al., 1999; Urban et al., 2009; Lambert et al., 2016;  
87 Ronsmans et al., 2018), but its relationship to PSCs still needs further investigation given the complexity  
88 of the nucleation mechanisms that depend on a series of parameters (e.g. atmospheric temperature, water  
89 and  $\text{HNO}_3$  vapour pressure, time exposure to temperatures, temperature history).

90  
91 In contrast to the limb satellite instruments mentioned above, the infrared nadir sounder IASI offers a  
92 dense spatial sampling of the entire globe, twice a day (Section 2). While it cannot provide a vertical  
93 profile of  $\text{HNO}_3$  similar to that from the limb sounders, IASI provides reliable total column  
94 measurements of  $\text{HNO}_3$  characterized by a maximum sensitivity in the low-middle stratosphere around  
95 50 hPa (20 km) during the dark Antarctic winter (Ronsmans et al., 2016, 2018) where PSCs form (Voigt  
96 et al., 2005; Lambert et al., 2012; Spang et al., 2016, 2018). This study aims to explore the 10-year  
97 continuous  $\text{HNO}_3$  measurements from IASI to provide a long-term global picture of depletion and of its

98 dependence to temperatures during polar winter (Section 3). The temperature corresponding to the onset  
99 of the strong depletion in HNO<sub>3</sub> records (here referred to as ‘drop temperature’) is identified in Section  
100 4 for each observed year and discussed in the context of previous studies.

## 101 102 **2 Data**

103  
104 The HNO<sub>3</sub> data used in the present study are obtained from measurements of the Infrared Atmospheric  
105 Sounding Interferometer (IASI) onboard the Metop-A satellite. IASI measures the Earth’s and  
106 atmosphere’s radiation in the thermal infrared spectral range (645 - 2760 cm<sup>-1</sup>), with a 0.5 cm<sup>-1</sup> apodized  
107 resolution and a low radiometric noise (Clerbaux et al., 2009; Hilton et al., 2012). Thanks to its polar  
108 sun-synchronous orbit with more than 14 orbits a day and a field of view of four simultaneous footprints  
109 of 12 km at nadir, IASI provides global coverage twice a day (9.30 AM and PM mean local solar time).  
110 That extensive spatial and temporal sampling in the polar regions is key to this study.

111  
112 The HNO<sub>3</sub> vertical profiles are retrieved on a uniform vertical 1 km grid of 41 layers (from the surface  
113 to 40 km with an extra layer above to 60 km) in near-real-time by the Fast Optimal Retrieval on Layers  
114 for IASI (FORLI) software, using the optimal estimation method (Rodgers, 2000). Detailed information  
115 on the FORLI algorithm and retrieval parameters specific to HNO<sub>3</sub> can be found in previous papers  
116 (Hurtmans et al., 2012; Ronsmans et al., 2016). For this study, only the total columns (v20151001) are  
117 used, considering (1) the low vertical resolution of IASI with only one independent piece of information  
118 (full width at half maximum - FWHM - of the averaging kernels of ~30 km), (2) the limited sensitivity  
119 of IASI to tropospheric HNO<sub>3</sub>, (3) the dominant contribution of the stratosphere to the HNO<sub>3</sub> total  
120 column and (4) the largest sensitivity of IASI in the region of interest, i.e. in the low and mid-stratosphere  
121 (from ~70 to ~30 hPa), where the HNO<sub>3</sub> abundance is the highest (Ronsmans et al., 2016). The IASI  
122 measurements capture the expected variations of HNO<sub>3</sub> within the polar night, as illustrated in Fig. 1  
123 that shows examples of vertical HNO<sub>3</sub> profiles retrieved within the dark Antarctic vortex (above Arrival  
124 Heights) and outside the vortex (above Lauder). The retrieved profiles are shown along with their  
125 associated total retrieval error and averaging kernels (the total column averaging kernel and the so-called  
126 “sensitivity profile” are also represented; see Ronsmans et al., 2016 for more details). The total column  
127 averaging kernel (in black) indicates the sensitivity of the total column measurement to changes in the  
128 vertical distribution of HNO<sub>3</sub>, hence, the altitude to which the retrieved total column is mainly  
129 sensitive/representative, while the sensitivity profile indicates to which extent the retrieval at one specific  
130 altitude comes from the spectral measurement rather than the a priori. Above Arrival Heights during the  
131 dark Antarctic winter, we clearly see depleted HNO<sub>3</sub> levels in the low and mid-stratosphere and the  
132 altitude of maximum sensitivity at around 30 hPa for this case (values of ~1 along the total column  
133 averaging kernel around that level). In contrast, at Lauder, HNO<sub>3</sub> levels larger than the a priori are  
134 observed in the stratosphere with a larger range of maximum sensitivity. The total columns are associated  
135 with a total retrieval error ranging from around 3% at mid- and polar latitudes (except above Antarctica)  
136 to 25% above cold Antarctic surface during winter (due to a weaker sensitivity above very cold surface  
137 with a degrees of freedom for signal (DOFS) of 0.95 and to a poor knowledge of the seasonally and  
138 wavenumber-dependent emissivity above ice surfaces which induces larger forward model errors), and  
139 a low absolute bias (smaller than 12%) in polar regions over the altitude range where the IASI sensitivity  
140 is the largest, when compared to ground-based FTIR measurements (see Hurtmans et al., 2012 and  
141 Ronsmans et al., 2016 for more details). In order to expand on the comparisons against FTIR  
142 measurements, which cannot be made during the polar night, Fig. 2 (top panel) presents the time series  
143 of daily IASI total HNO<sub>3</sub> columns co-located with MLS measurements within 2.5°x2.5° grid boxes,  
144 averaged in the 70°S–90°S equivalent latitude band. In order to account for the vertical sensitivity of  
145 IASI, the averaging kernels associated with each co-located IASI retrieved profiles were applied to the  
146 MLS profiles for this cross-comparison. The MLS VMR profiles over the 215-1.5 hPa pressure range

147 were first interpolated to the FORLI pressure grids and extended down to the surface by using the  
148 FORLI-HNO<sub>3</sub> a priori profile, and then converted into partial columns. Similar variations in the HNO<sub>3</sub>  
149 column are captured by the two instruments, with an excellent agreement in particular for the timing of  
150 the strong HNO<sub>3</sub> depletion within the inner vortex core. Note that a similar good agreement between the  
151 two satellite datasets is obtained in other latitude bands (see Fig. 2 bottom panel for the 50°S–70°S  
152 equivalent latitude band; the other bands are not shown).

153  
154 Quality flags similar to those developed for O<sub>3</sub> in previous IASI studies (Wespes et al., 2017) were  
155 applied a posteriori to exclude data (i) with a corresponding poor spectral fit (e.g. based on quality flags  
156 rejecting biased or sloped residuals, fits with maximum number of iteration exceeded), (ii) with less  
157 reliability (e.g. based on quality flags rejecting suspect averaging kernels, data with less sensitivity  
158 characterized by a DOFS lower than 0.9) or (iii) with tropospheric cloud contamination (defined by a  
159 fractional cloud cover  $\geq 25$  %). Note that the HNO<sub>3</sub> total column distributions illustrated in sections  
160 below use the median as a statistical average since it is more robust against the outliers than the mean.

161  
162 Temperature and potential vorticity (PV) fields are taken from the ECMWF ERA Interim Reanalysis  
163 dataset, respectively at 50 hPa and at the potential temperature of 530 K (corresponding to ~20 km  
164 altitude where the IASI sensitivity to HNO<sub>3</sub> is the highest during the Southern Hemisphere (S.H.) winter  
165 (Ronsmans et al., 2016)). Because the HNO<sub>3</sub> uptake by PSCs starts within a few degrees below  $T_{NAT}$   
166 (~195.7 K at 50 hPa (Hanson and Mauersberger, 1988)) depending on the meteorological conditions  
167 (Pitts et al., 2013; Hoyle et al., 2013; Lambert et al., 2016; Pitts et al., 2018), a threshold temperature of  
168 195 K is considered in the sections below to identify regions of potential PSC existence. The potential  
169 vorticity is used to delimit dynamically consistent areas in the polar regions. In what follows, we use  
170 either the equivalent latitudes ("eqlat", calculated from PV fields at 530 K) or the PV values to  
171 characterize the relationship between HNO<sub>3</sub> and temperatures in the cold polar regions. Uncertainties in  
172 ERA-Interim temperatures will also be discussed below.

### 173 174 **3 Annual cycle of HNO<sub>3</sub> vs temperatures**

175  
176 Figure 3a shows the yearly HNO<sub>3</sub> cycle (solid lines, left axis) in the southernmost equivalent latitudes  
177 (70° - 90° S) as measured by IASI over the whole study period (2008–2017). The total HNO<sub>3</sub> variability  
178 in such equivalent latitudes has already been discussed in a previous IASI study (Ronsmans et al., 2018),  
179 where the contribution of the PSCs to the HNO<sub>3</sub> variations was highlighted. The temperature time series,  
180 taken at 50 hPa, is represented as well (dashed lines, right axis). From this figure, different regimes of  
181 HNO<sub>3</sub> total columns vs temperature can be observed throughout the year and from one year to another.  
182 In particular, we define here three main regimes (R1, R2 and R3) during the HNO<sub>3</sub>/temperature annual  
183 cycle. The full cycle and the main regimes in the 70° - 90° S eqlat region are further represented in Fig.  
184 3b that shows a histogram of the HNO<sub>3</sub> total columns as a function of temperature for the year 2011.  
185 Similar histograms are observed for the ten years of IASI measurements (not shown). The red horizontal  
186 and vertical lines in Fig. 3a and Fig. 3b, respectively, represent the 195 K threshold temperature used to  
187 identify the onset of HNO<sub>3</sub> uptake by PSCs (see Section 2). The three identified regimes correspond to:

- 188  
189 - R1 is defined by the maxima in the total HNO<sub>3</sub> abundances covering the months of April and  
190 May ( $\sim 3 \times 10^{16}$  molec.cm<sup>-2</sup>), when the 50 hPa temperature strongly decreases (from ~220 to ~195  
191 K). These high HNO<sub>3</sub> levels result from low sunlight, preventing photodissociation, along with  
192 the heterogeneous hydrolysis of N<sub>2</sub>O<sub>5</sub> to HNO<sub>3</sub> during autumn before the formation of polar  
193 stratospheric clouds (Keys et al., 1993; Santee et al., 1999; Urban et al., 2009; de Zafra and  
194 Smyshlyaev, 2001). This period also corresponds to the onset of the development of the southern

195 polar vortex, which is characterized by strong diabatic descent with weak latitudinal mixing  
196 across its boundary, isolating polar HNO<sub>3</sub>-rich air from lower-latitude airmasses.

197

198 - R2, which extends from June to October, follows the onset of the strong decrease in HNO<sub>3</sub> total  
199 columns which starts around mid-May in most years when the temperatures fall below 195 K,  
200 and is characterized by a plateau of total HNO<sub>3</sub> minima. In this regime, average HNO<sub>3</sub> total  
201 columns are below  $2 \times 10^{16}$  molec.cm<sup>-2</sup> and the 50 hPa temperatures range mostly between 180  
202 and 190 K.

203

204 - R3 starts in October when sunlight returns and the 50 hPa temperatures rise above 195 K. Despite  
205 50 hPa temperatures increasing up to 240 K in summer, the HNO<sub>3</sub> total columns stagnate at the  
206 R2 plateau levels (around  $1.5 \times 10^{16}$  molec.cm<sup>-2</sup>). This regime likely reflects the photolysis of NO<sub>3</sub>  
207 and HNO<sub>3</sub> itself (Ronsmans et al., 2018) as well as the permanent denitrification of the mid-  
208 stratosphere, caused by sedimentation of PSCs. The likely reinitiation of the lowermost  
209 stratosphere (e.g. Braun et al., 2019; Lambert et al., 2012), where the HNO<sub>3</sub> concentrations and  
210 the IASI sensitivity to HNO<sub>3</sub> are lower (Ronsmans et al., 2016), cannot be inferred from the IASI  
211 total column measurements. The plateau lasts until approximately February, when HNO<sub>3</sub> total  
212 column slowly starts increasing, reaching the April-May maximum in R1.

213

214 As illustrated in Fig. 3a, the three regimes are observed each year with, however, some interannual  
215 variations. For instance, the sudden stratospheric warming (SSW) that occurred in 2010 (see the  
216 temperature time series at 20 hPa for the year 2010; green dotted line) yielded higher HNO<sub>3</sub> total columns  
217 (see green solid line in July - September) (de Laat and van Weele, 2011; Klekociuk et al., 2011; WMO,  
218 2014; Ronsmans et al., 2018).

219

220 Figure 3c shows the evolution of the relationship between the daily averaged HNO<sub>3</sub> (calculated from a  
221 7-day moving average) with the highest occurrence (in bins of  $0.1 \times 10^{16}$  molec.cm<sup>-2</sup> and of 2K) and the  
222 50 hPa temperature, over the 10 years of IASI. The red vertical line represents the 195 K threshold  
223 temperature. Figure 3c clearly illustrates the slow increase in HNO<sub>3</sub> columns as the temperatures  
224 decrease (February to May, i.e. R3 to R1), the strong and rapid HNO<sub>3</sub> depletion occurring in June (R2),  
225 and the plateau of low HNO<sub>3</sub> abundances in winter and spring (from July to November; R2 to R3).  
226 Figure 3c also highlights a large interannual variability in total HNO<sub>3</sub> in R3, while the strong depletion  
227 in HNO<sub>3</sub> in R2 is consistent every year (beginning of June when the temperatures fall below 195 K as  
228 indicated by the red vertical line). Given that PSC formation spans a large range of altitudes (typically  
229 between 10 and 30 km) (Höpfner et al., 2006, 2009; Spang et al., 2018; Pitts et al., 2018) and that IASI  
230 has maximum sensitivity to HNO<sub>3</sub> around 50 hPa (Hurtmans et al., 2012; Ronsmans et al., 2016), the  
231 temperatures at two other pressure levels, namely 70 and 30 hPa (i.e. ~15 and ~25 km), have also been  
232 tested to investigate the relationship between HNO<sub>3</sub> and temperature in the low and mid-stratosphere.  
233 The results (not shown here) exhibit a similar HNO<sub>3</sub>-temperature behavior at the different levels with,  
234 as expected, lower and higher temperatures in R2, respectively, at 30 hPa and at 70 hPa (temperatures  
235 down to ~180 K at 30 hPa and down to ~185 K at 70 hPa, as compared to temperatures down to ~182 K  
236 at 50 hPa, are observed), but still below the NAT formation threshold at these pressure levels ( $T_{NAT} \sim 193$   
237 K at 30 hPa and ~197 K at 70 hPa) (Lambert et al., 2016). Therefore, the altitude range of maximum  
238 IASI sensitivity to HNO<sub>3</sub> (see Section 2) is characterized by temperatures that are below the NAT  
239 formation threshold at these pressure levels, enabling PSC formation and the denitrification process.  
240 Furthermore, the consistency between the 195 K threshold temperature taken at 50 hPa and the onset of  
241 the strong total HNO<sub>3</sub> depletion seen in IASI data (see Fig. 3a) is in agreement with the largest NAT  
242 area that starts to develop in June around 20 km (Spang et al., 2018), which justifies the use of the 195  
243 K temperature at that single representative level in this study.

244  
245  
246  
247  
248  
249  
250  
251  
252  
253  
254  
255  
256  
257  
258  
259  
260  
261  
262  
263  
264  
265  
266  
267  
268  
269  
270  
271  
272  
273  
274  
275  
276  
277  
278  
279  
280  
281  
282  
283  
284  
285  
286  
287  
288  
289  
290  
291  
292

## 4 Onset of HNO<sub>3</sub> depletion and drop temperature detection

To identify the spatial and temporal variability of the onset of the depletion phase, the daily time evolution of HNO<sub>3</sub> during the first 10 years of IASI measurements and the temperatures at 50 hPa are explored. In particular, the second derivative of HNO<sub>3</sub> total column with respect to time is calculated to detect the strongest rate of decrease seen in the HNO<sub>3</sub> time series and to identify its associated day and 50 hPa temperature.

### 4.1 HNO<sub>3</sub> vs temperature time series

Figure 4 shows the time series of the second derivative of HNO<sub>3</sub> total column with respect to time (blue) and of the temperature (red) averaged in the area of potential vorticity at the potential temperature of 530 K smaller than  $-10 \times 10^{-5} \text{ K.m}^2.\text{kg}^{-1}.\text{s}^{-1}$  to encompass the region inside the inner polar vortex where the temperatures are the coldest and the largest depletion of total HNO<sub>3</sub> occurs (Ronsmans et al., 2018). The use of that PV threshold value explains the gaps in the time series during the summer when the PV does not reach such low levels, while the time series averaged in the 70°- 90° S Eqlat band (dashed blue for the second derivative of HNO<sub>3</sub> and grey for the temperature) covers the full year. Note that the HNO<sub>3</sub> time series has been smoothed with a simple spline data interpolation function to avoid gaps in order to calculate the second derivative of HNO<sub>3</sub> total column with respect to time as the daily second-difference in HNO<sub>3</sub> total columns. The horizontal red line shows the 195 K threshold.

As already illustrated in Fig. 3a and Fig. 3c, the strongest rate of HNO<sub>3</sub> depletion (i.e. the second derivative minimum) is found around the time that temperatures drop below the 195 K threshold, within a few days to a few weeks (4 to 23 days) after total HNO<sub>3</sub> reaches its maximum, i.e. between the 12th of May (2013) and the 8th of June (2009). The 50 hPa drop temperatures, i.e. the temperature associated with the strongest HNO<sub>3</sub> depletion detected from IASI, are detected between 189.2 K and 198.6 K with an exception for the year 2014 which shows a drop temperature of 202.8 K. On average over the 10 years of studied IASI measurements, a 50 hPa drop temperature of  $194.2 \text{ K} \pm 3.8 \text{ K}$  ( $1\sigma$  standard deviation) is found. Knowing that  $T_{\text{NAT}}$  can be higher or lower depending on the atmospheric conditions and that NAT starts to nucleate from  $\sim 2-4 \text{ K}$  below  $T_{\text{NAT}}$  (Pitts et al., 2011; Hoyle et al., 2013; Lambert et al., 2016), the results here tend to demonstrate the consistency between the 50 hPa drop temperature and the PSC existence temperature in that altitude region. Note that the range observed in the 50 hPa drop temperature could reflect variations in the preponderance of one type of PSCs over another from one year to the next. The results further justify the use of the single 50 hPa level for characterizing and investigating the onset of HNO<sub>3</sub> depletion from IASI. Nevertheless, given the range of maximum IASI sensitivity to HNO<sub>3</sub> around 50 hPa, typically between 70 and 30 hPa (Ronsmans et al., 2016), the drop temperatures are also calculated at these two other pressure levels (not shown here) in order to estimate the uncertainty of the calculated drop temperature defined in this study at 50 hPa. The 30 hPa and 70 hPa drop temperatures range respectively over 185.7 K – 194.9 K and over 194.8 K – 203.7 K, with an average of  $192.0 \pm 2.9 \text{ K}$  and  $198.0 \pm 3.2 \text{ K}$  ( $1\sigma$  standard deviation) over the ten years of IASI. The average values at 30 hPa and 70 hPa fall within the  $1\sigma$  standard deviation associated with the average drop temperature at 50 hPa. It is also worth noting the agreement between the drop temperatures and the NAT formation threshold at these two pressure levels ( $T_{\text{NAT}} \sim 193 \text{ K}$  at 30 hPa and  $\sim 197 \text{ K}$  at 70 hPa) (Lambert et al., 2016). Finally, it should be noted that, because the size, shape or location of the vortex vary slightly over the altitude range to which IASI is sensitive (from  $\sim 30$  to  $\sim 70$  hPa during the polar night), the use of a single potential temperature surface for the calculation of drop temperatures could introduce some uncertainties into the results. However, several tests suggest that these variations of the vortex are overall minor and, hence, could only have limited influence on the delimitation of the inner

293 polar vortex (delimited by a PV value of  $-10 \times 10^{-5} \text{K.m}^2.\text{kg}^{-1}.\text{s}^{-1}$  at 530 K) and on the detection of the  
294 average drop temperature inside that region.

295

296 Figures 5a and b show the climatological zonal distribution of  $\text{HNO}_3$  total columns and of the  
297 temperature at 50 hPa, respectively, spanning the  $55^\circ \text{S} - 90^\circ \text{S}$  geographic latitude band over the whole  
298 IASI period, with, superimposed, three isocontour levels of potential vorticity ( $-10$ ,  $-8$  and  $-5 \times 10^{-5}$   
299  $\text{K.m}^2.\text{kg}^{-1}.\text{s}^{-1}$  in blue, cyan and black, respectively) and the isocontours for the 195 K temperature (pink) and  
300 for the averaged 194.2 K drop temperature (purple) at 50 hPa. They further illustrate the relationship between  
301 the IASI total  $\text{HNO}_3$  columns and the 50 hPa temperatures. The average PV isocontour of  $-10 \times 10^{-5}$   
302  $\text{K.m}^2.\text{kg}^{-1}.\text{s}^{-1}$  is clearly shown to separate well the region of strong depletion in total  $\text{HNO}_3$  according to  
303 the latitude and the time. The red vertical dashed line indicates the average date for the 50 hPa average  
304 drop temperatures calculated in the area of  $\text{PV} \leq -10 \times 10^{-5} \text{K.m}^2.\text{kg}^{-1}.\text{s}^{-1}$  ( $194.2 \pm 3.8 \text{K}$ ; see Fig. 4) over  
305 the IASI period. It shows that the strongest rate of  $\text{HNO}_3$  depletion occurs on average end of May, a few  
306 days after the temperature decreases below 195 K. The delay between the maximum in total  $\text{HNO}_3$  and  
307 the start of the depletion (see Fig. 4) is also visible in Fig. 5a. For the purpose of the illustrations, the  
308 yearly zonally averaged time series over the ten years of IASI can be found in Fig. 6; it shows the  
309 reproducibility of the edge of the collar  $\text{HNO}_3$  region and of the region of the strong  $\text{HNO}_3$  depletion,  
310 respectively delimited by the PV isocontours of  $-5 \times 10^{-5} \text{K.m}^2.\text{kg}^{-1}.\text{s}^{-1}$  and of  $-10 \times 10^{-5} \text{K.m}^2.\text{kg}^{-1}.\text{s}^{-1}$  at  
311 530 K, measured by IASI from year to year, as well as the reproducibility of the NAT threshold  
312 temperature region that encompasses the inner vortex core. Except for the year 2009, the dates for the  
313 strongest rate of  $\text{HNO}_3$  depletion matches those for the onset of decreasing temperatures below 195 K.

314

#### 315 **4.2 Distribution of drop temperatures**

316

317 To explore the capability of IASI to monitor the onset of  $\text{HNO}_3$  depletion at a large scale from year to  
318 year, figure 7 shows the spatial distribution of the 50 hPa drop temperatures (based on the second  
319 derivative minima of total  $\text{HNO}_3$  averaged in  $1^\circ \times 1^\circ$  grid cells) inside a region delimited by a PV value  
320 of  $-8 \times 10^{-5} \text{K.m}^2.\text{kg}^{-1}.\text{s}^{-1}$  for each year of the IASI period in order to investigate a region a bit larger than  
321 that of the strong depletion in total  $\text{HNO}_3$  encircled by the PV isocontour of  $-10 \times 10^{-5} \text{K.m}^2.\text{kg}^{-1}.\text{s}^{-1}$ ,  
322 averaged over the 10 May – 15 July period for each year, which delimits our region of interest (in green).  
323 The isocontour of  $-10 \times 10^{-5} \text{K.m}^2.\text{kg}^{-1}.\text{s}^{-1}$  for the minimum PV (in cyan) encountered at 530 K over the  
324 10 May to 15 July period for each year, as well as the isocontours of 195 K for the average temperatures  
325 and the minimum temperatures, are also represented. The calculated drop temperatures corresponding  
326 to the onset of  $\text{HNO}_3$  depletion inside the averaged PV isocontour are found to vary between  $\sim 180$  and  
327  $\sim 210 \text{K}$  and the corresponding dates range between  $\sim$ mid-May and mid-July (not shown here). The year  
328 2014 that shows the highest average drop temperature in Figure 4 is characterized by the highest drop  
329 temperatures above the eastern Antarctic. Note, however, that the high extremes in the drop temperature,  
330 mainly found above the eastern Antarctic, should be considered with caution: they correspond to specific  
331 regions above ice surfaces with emissivity features that are known to yield errors in the IASI retrievals  
332 (Hurtmans et al., 2012; Ronsmans et al., 2016). Indeed, bright land surfaces such as ice might in some  
333 cases lead to poor  $\text{HNO}_3$  retrievals. Although wavenumber-dependent surface emissivity atlases are used  
334 in FORLI (Hurtmans et al., 2012), this parameter remains critical and causes poorer retrievals that, in  
335 some instances, pass through the series of quality filters and could affect the drop temperature  
336 calculation.

337

338 The averaged isocontour of 195 K encircles fairly well the area of  $\text{HNO}_3$  drop temperatures lower than  
339 195 K (typically from  $\sim 187 \text{K}$  to  $\sim 195 \text{K}$ ), which means that the bins inside that area include airmasses  
340 that experience the NAT threshold temperature during a long time over the 10 May – 15 July period.  
341 That area encompasses the inner vortex core (delimited by the isocontour of  $-10 \times 10^{-5} \text{K.m}^2.\text{kg}^{-1}.\text{s}^{-1}$  for

342 the PV averaged over the 10 May – 15 July period) and shows pronounced minima (lower than  $-0.5 \times 10^{14}$   
343 molec.cm<sup>-2</sup>.d<sup>-2</sup>) in the second derivative of the HNO<sub>3</sub> total column with respect to time (not shown here),  
344 which indicate a strong and rapid HNO<sub>3</sub> depletion. The area enclosed between the two isocontours of  
345 195 K for the temperatures, the averaged one and the one for the minimum temperatures, shows generally  
346 higher drop temperatures and weakest minima (larger than  $-0.5 \times 10^{14}$  molec.cm<sup>-2</sup>.d<sup>-2</sup>) in the second  
347 derivative of the HNO<sub>3</sub> total column (not shown). That area is also typically enclosed by the isocontour  
348 of  $-10 \times 10^{-5}$  K.m<sup>2</sup>.kg<sup>-1</sup>.s<sup>-1</sup> for the minimum PV, meaning that the bins inside correspond, at least for one  
349 day over the 10 May – 15 July period, to airmasses located at the inner edge of the vortex and  
350 characterized by temperature lower than the NAT threshold temperature. The fact that the weakest  
351 minima in the second derivative of total HNO<sub>3</sub> (not shown) are observed in that area indicates a weak  
352 and slow HNO<sub>3</sub> depletion and might be explained by a short period of the NAT threshold temperature  
353 experienced at the inner edge of the vortex. It could also reflect mixing with strongly HNO<sub>3</sub>-depleted  
354 and colder airmasses from the inner vortex core. Mixing with these already depleted airmasses could  
355 also explain the higher drop temperatures detected in those bins. These sometimes unrealistic high drop  
356 temperatures are generally detected later (after the strong HNO<sub>3</sub> depletion occurs in the inner vortex  
357 core, i.e. after the 10 May – 15 July period considered here – not shown), which supports the transport,  
358 in those bins, of earlier HNO<sub>3</sub>-depleted airmasses and the likely mixing at the edge of the vortex. Note,  
359 however, that previous studies have shown a generally weak mixing in the Antarctic between the edge  
360 region and the vortex core (e.g. Roscoe et al., JGR 2012). Finally, these spatial variations might also  
361 partly reflect some uncertainty into the drop temperature calculation, introduced by the use of  
362 temperature at a single pressure level (50 hPa) and of PV on a single potential temperature surface (530  
363 K) while the sensitivity of IASI to changes in the HNO<sub>3</sub> profiles extends over a range from ~30 to ~70  
364 hPa during the polar night. It should be note that biases in the ECMWF ERA Interim temperatures used  
365 in this work, are too small to explain the large range of drop temperatures calculated here. Indeed,  
366 Lambert and Santee (2018) found a small warm bias, with median differences around 0.5 K, reaching  
367 0–0.25 K in the southernmost regions of the globe at ~68–21 hPa where PSCs form, through comparisons  
368 with the COSMIC data.

369  
370 Except above some parts of Antarctica which are prone to larger retrieval errors and where unrealistic  
371 high drop temperatures are found, the overall range in the 50 hPa drop temperature for total HNO<sub>3</sub> inside  
372 the isocontour for the averaged temperature of 195 K typically extends from ~187 K to ~195 K, which  
373 falls within the range of PSC nucleation temperature at 50 hPa: from slightly below  $T_{NAT}$  to around 3–4  
374 K below the ice frost point -  $T_{ice}$  - depending on atmospheric conditions, on TTE and on the specific  
375 formation mechanism (i.e., the type of PSC developing) (Pitts et al., 2011; Peter and Grooß, 2012; Hoyle  
376 et al., 2013). This underlines well the benefit of the excellent spatial and temporal coverage of IASI,  
377 which allows the rapid and critical depletion phase to be captured in detail over a large scale.

## 378 379 **5 Conclusions**

380  
381 In this paper, we have explored the added value of the dense HNO<sub>3</sub> total column dataset provided by the  
382 IASI/Metop-A satellite over a full decade (2008–2017) for monitoring the stratospheric depletion phase  
383 that occurs each year in the S.H. and for investigating its relationship to the NAT formation temperature.  
384 To that end, we focused on and delimited the coldest polar region of the S.H. using a specific PV value  
385 at 530 K (~50 hPa, PV of  $-10 \times 10^{-5}$  K.m<sup>2</sup>.kg<sup>-1</sup>.s<sup>-1</sup>) and stratospheric temperatures at 50 hPa, taken from  
386 the ECMWF ERA Interim reanalysis. That single representative pressure level has been considered in  
387 this study given the maximum sensitivity of IASI to HNO<sub>3</sub> around that level, which lies in the range  
388 where the PSCs formation/denitrification processes occur.  
389



390 The annual cycle of total HNO<sub>3</sub>, as observed from IASI, has first been characterized according to the  
391 temperature evolution. Three regimes (R1 to R3) in the total HNO<sub>3</sub> - 50 hPa temperature relationship  
392 were highlighted from the time series over the S.H. polar region: R1 is defined during April and May  
393 and characterized by a rapid decrease in 50 hPa temperatures while HNO<sub>3</sub> accumulates in the poles; R2,  
394 from June to September, follows the onset of the depletion that starts around mid-May in most years  
395 when the 50 hPa temperatures fall below 195 K (considered here as the onset of PSC nucleation phase  
396 at that level), with a strong consistency from year to year; R3, defined from October through March  
397 when total HNO<sub>3</sub> remains at low R2 plateau levels, despite the return of sunlight and heat, characterizes  
398 the strong denitrification of the stratosphere, likely due to PSC sedimentation to lower levels where the  
399 IASI sensitivity is low. For each year over the IASI period, the use of the second derivative of the HNO<sub>3</sub>  
400 column versus time was then found to be particularly valuable to detect the onset of the HNO<sub>3</sub>  
401 condensation into PSCs. It is captured, on average from IASI, a few days before June with a delay of 4–  
402 23 days after the maximum in total HNO<sub>3</sub>. The corresponding temperatures ('drop temperatures') were  
403 detected between 189.2 K and 202.8 K ( $194.2 \pm 3.8$  on average over the 10 years), which tends to  
404 demonstrate the good consistency between the 50 hPa drop temperature and the PSC formation  
405 temperatures in that altitude region. Finally, the annual and spatial variability (within  $1^\circ \times 1^\circ$ ) in the drop  
406 temperature was further explored from IASI total HNO<sub>3</sub>. Inside the isocontours of 195 K for the average  
407 temperatures and of  $-10 \times 10^{-5} \text{ K.m}^2.\text{kg}^{-1}.\text{s}^{-1}$  for the averaged PV at 530 K, the drop temperatures are  
408 detected between ~mid-May and mid-July, typically range between ~187 K to ~195 K and are associated  
409 with the lowest minima (lower than  $-0.5 \times 10^{14} \text{ molec.cm}^{-2}.\text{d}^{-2}$ ) in the second derivative of the HNO<sub>3</sub> total  
410 column with respect to time, indicating a strong and rapid HNO<sub>3</sub> depletion. Except for extreme drop  
411 temperatures (~210 K) that were found in some years above eastern Antarctica and suspected to result  
412 from unfiltered poor quality retrievals in case of emissivity issues above ice, the range of drop  
413 temperatures is interestingly found to be in line with the PSC nucleation temperature that is known, from  
414 previous studies, to strongly depend on a series of factors (e.g. meteorological conditions, HNO<sub>3</sub> vapour  
415 pressure, temperature threshold exposure, presence of meteoritic dust). At the edge of the vortex,  
416 considering the isocontours of 195 K for the minimum temperatures or of  $-10 \times 10^{-5} \text{ K.m}^2.\text{kg}^{-1}.\text{s}^{-1}$  for the  
417 minimum PV, higher and later drop temperatures along with weakest minima in the second derivative  
418 of the HNO<sub>3</sub> total column with respect to time, indicating a slow HNO<sub>3</sub> depletion, are found. These  
419 likely results from a short temperature threshold exposure or mixing with already depleted airmasses  
420 from the inner vortex core. The results of this study highlight the ability of IASI to measure the variations  
421 in total HNO<sub>3</sub> and, in particular, to capture and monitor the rapid depletion phase over the whole  
422 Antarctic regions.

423  
424 We show in this study that the IASI dataset allows the variability of stratospheric HNO<sub>3</sub> throughout the  
425 year (including the polar night) in the Antarctic to be captured. In that respect, it offers observational  
426 means to monitor the relation of HNO<sub>3</sub> to temperature and the related formation of PSCs. Despite the  
427 limited vertical resolution of IASI which does not allow investigation of the HNO<sub>3</sub> uptake by the  
428 different types of PSCs during their formation and growth along the vertical profile, the HNO<sub>3</sub> total  
429 column measurements from IASI constitute an important new dataset for exploring the strong polar  
430 depletion over the whole stratosphere. This is particularly relevant considering the mission continuity,  
431 which will span several decades with the planned follow-on missions. Indeed, thanks to the three  
432 successive instruments (IASI-A launched in 2006 and still operating, IASI-B in 2012, and IASI-C in  
433 2018) that demonstrate an excellent stability of the Level-1 radiances, the measurements will soon  
434 provide an unprecedented long-term dataset of HNO<sub>3</sub> total columns. Further work could also make use  
435 of this unique data set to investigate the relation between HNO<sub>3</sub>, O<sub>3</sub>, and meteorology in the changing  
436 climate.

437  
438

439  
440  
441  
442  
443  
444  
445  
446  
447  
448  
449  
450  
451  
452  
453  
454  
455  
456  
457  
458  
459  
460  
461  
462  
463  
464  
465  
466  
467  
468  
469  
470  
471  
472  
473  
474  
475  
476  
477  
478  
479  
480  
481  
482  
483  
484  
485  
486  
487

**Data availability**

The IASI HNO<sub>3</sub> data processed with FORLI-HNO<sub>3</sub> v0151001 are available upon request to the corresponding author.

**Author contributions**

G.R. performed the analysis, wrote the manuscript and prepared the figures. C.W. and L.C. contributed to the analysis. C.W., S.S., P.-F. C. and L.C. contributed to the interpretation of the results. D.H. was responsible for the retrieval algorithm development and the processing of the IASI HNO<sub>3</sub> dataset. All authors contributed to the writing of the text and reviewed the manuscript.

**Competing interests**

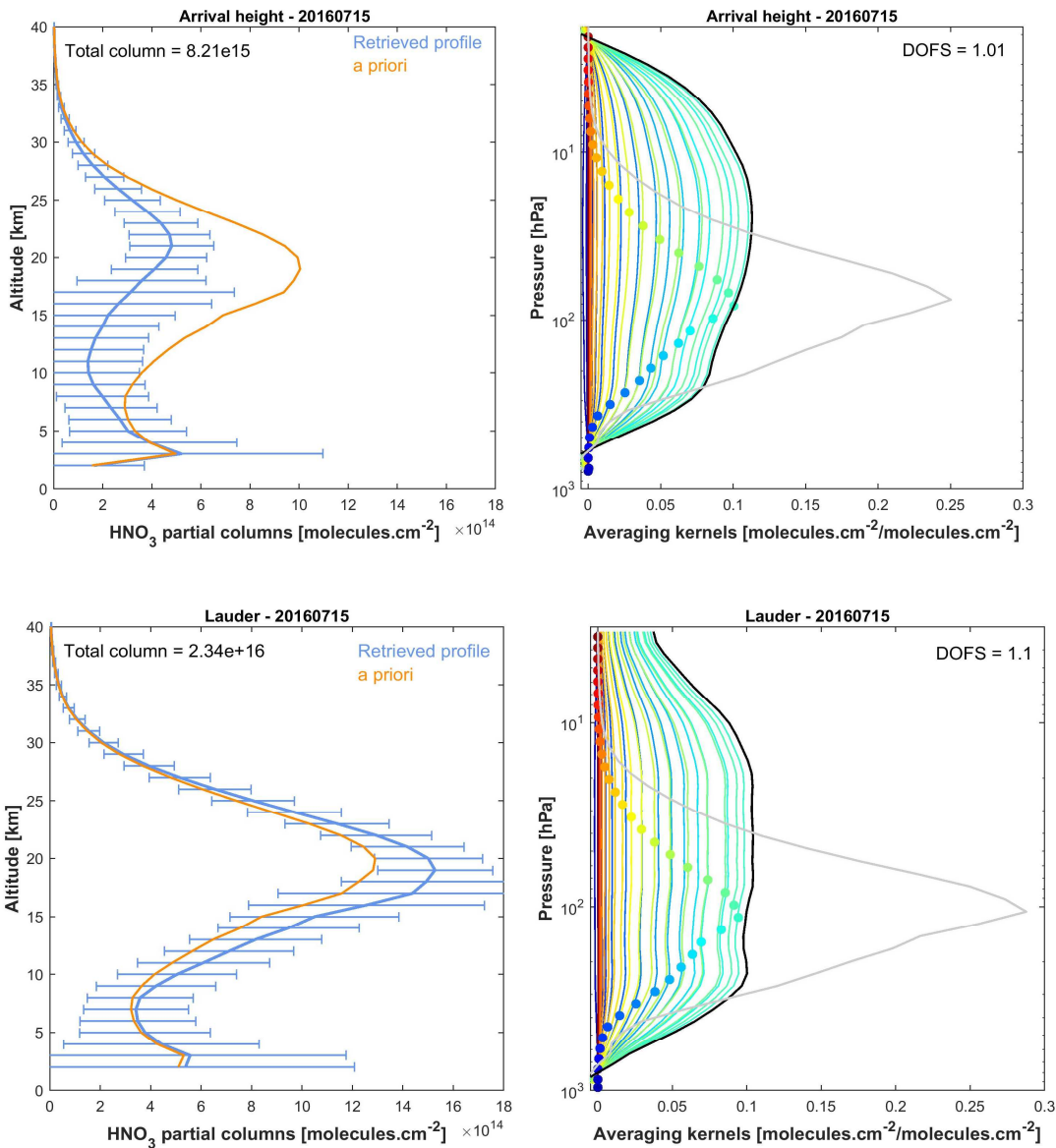
The authors declare no competing interests.

**Acknowledgements**

IASI has been developed and built under the responsibility of the Centre National d'Etudes Spatiales (CNES, France). It is flown on board the Metop satellites as part of the EUMETSAT Polar System. The IASI L1 data are received through the EUMETCast near-real-time data distribution service. The research was funded by the F.R.S.-FNRS, the Belgian State Federal Office for Scientific, Technical and Cultural Affairs (Prodex arrangement 4000111403 IASI.FLOW) and EUMETSAT through the Satellite Application Facility on Atmospheric Composition Monitoring (ACSAF). G. Ronsmans is grateful to the Fonds pour la Formation à la Recherche dans l'Industrie et dans l'Agriculture of Belgium for a PhD grant (Boursier FRIA). L. Clarisse is a research associate supported by the F.R.S.-FNRS. C. Clerbaux is grateful to CNES for financial support. S. Solomon is supported by the National Science Foundation (NSF-1539972).

488  
489

## Figure captions

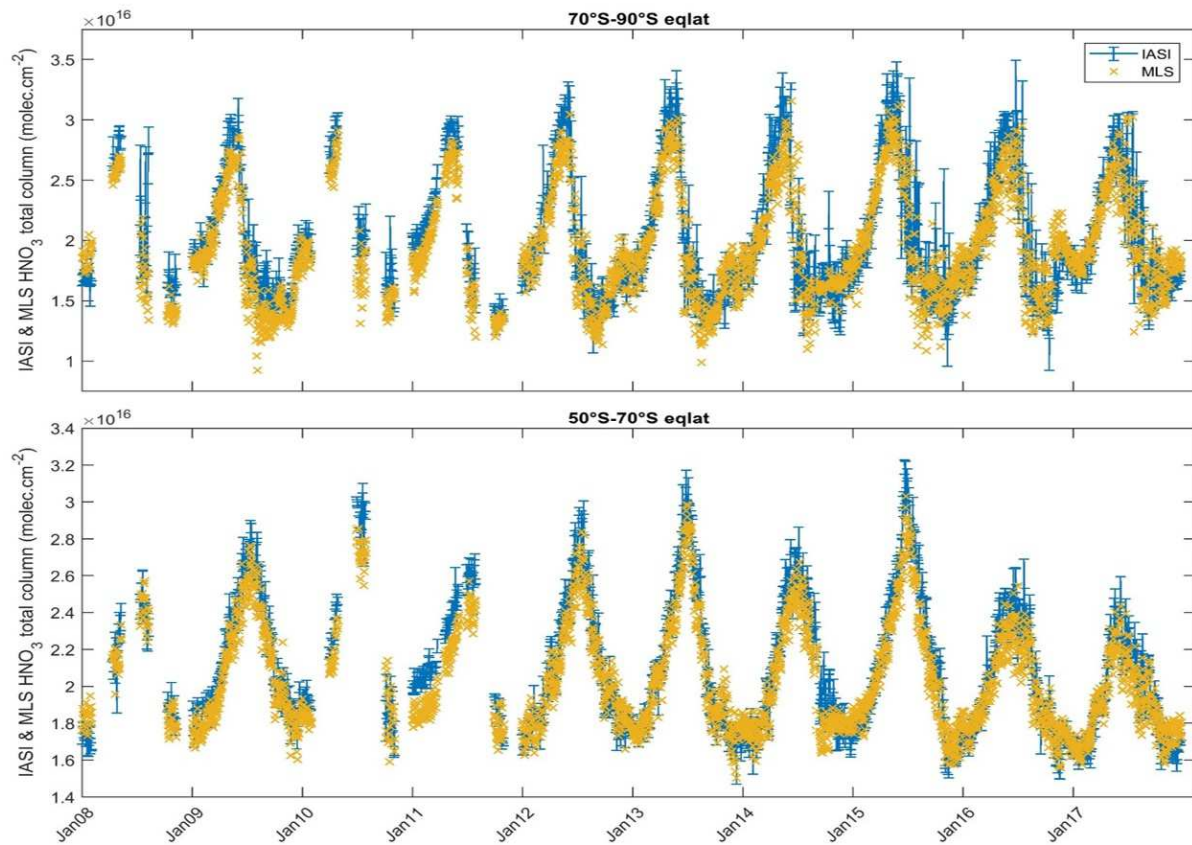


491

492  
493

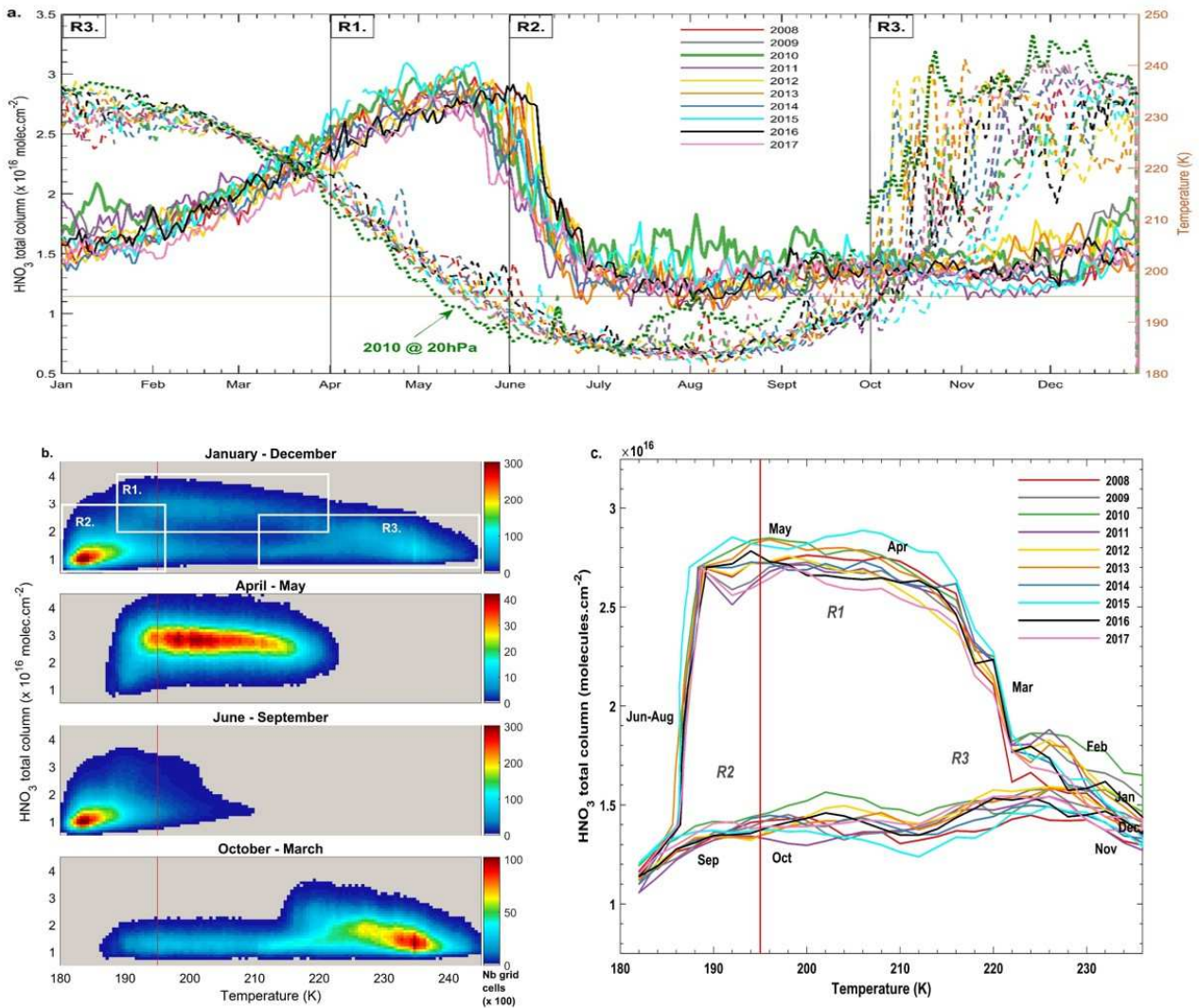
494 Figure 1. Examples of IASI HNO<sub>3</sub> vertical profiles (in molec.cm<sup>-2</sup>) with corresponding averaging kernels (in  
495 molec.cm<sup>-2</sup>/molec.cm<sup>-2</sup>; colored lines, with the altitude of each kernel represented by the colored dots)  
496 along with the total column averaging kernels (black) and the sensitivity profiles (grey) (divided by 10) above  
497 Arrival Heights (77.49°S, 166.39°E, top panels) and Lauder (45.03°S, 169.40°E; bottom panels). The error bars  
498 associated with the HNO<sub>3</sub> vertical profile represent the total retrieval error. The a priori profile is also represented.  
499 The total column and the DOFS values are indicated.

500



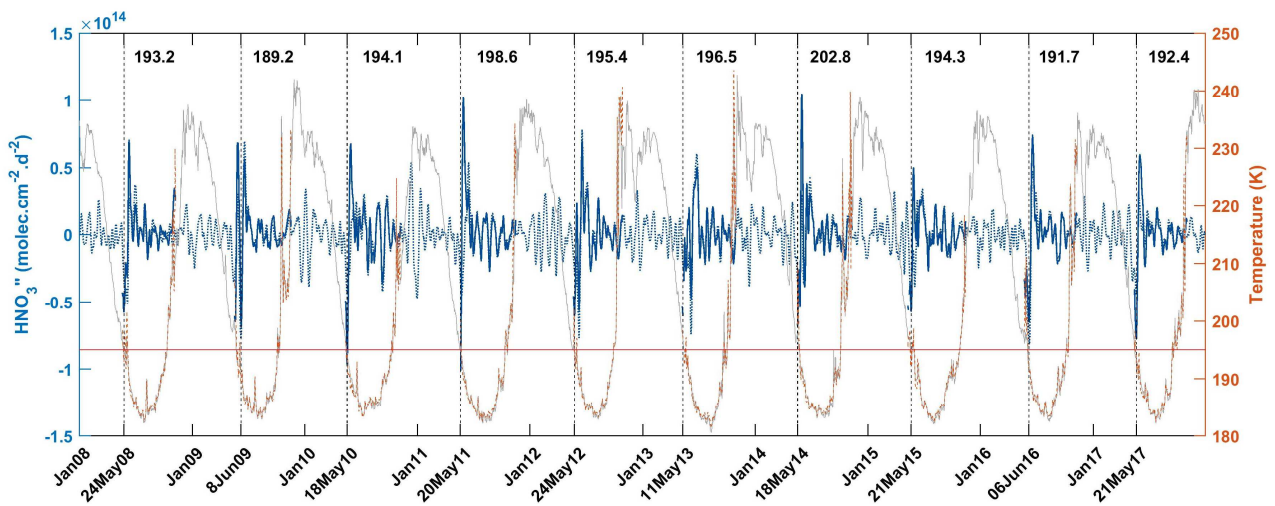
501  
 502  
 503  
 504  
 505  
 506  
 507  
 508  
 509  
 510  
 511  
 512  
 513  
 514  
 515

**Figure 2.** Time series of daily IASI total HNO<sub>3</sub> column (blue) co-located with MLS and of MLS total HNO<sub>3</sub> columns (orange) within 2.5°x2.5° grid boxes, averaged in the 70°S–90°S (top panel) and the 50°S–70°S (bottom panel) equivalent latitude bands. Note that the MLS total column estimates were obtained by extending the MLS partial stratospheric column values using the FORLI-HNO<sub>3</sub> a priori information (see text for details). The error bars (blue) represents 3σ, where σ is the standard deviation around the IASI HNO<sub>3</sub> daily average.



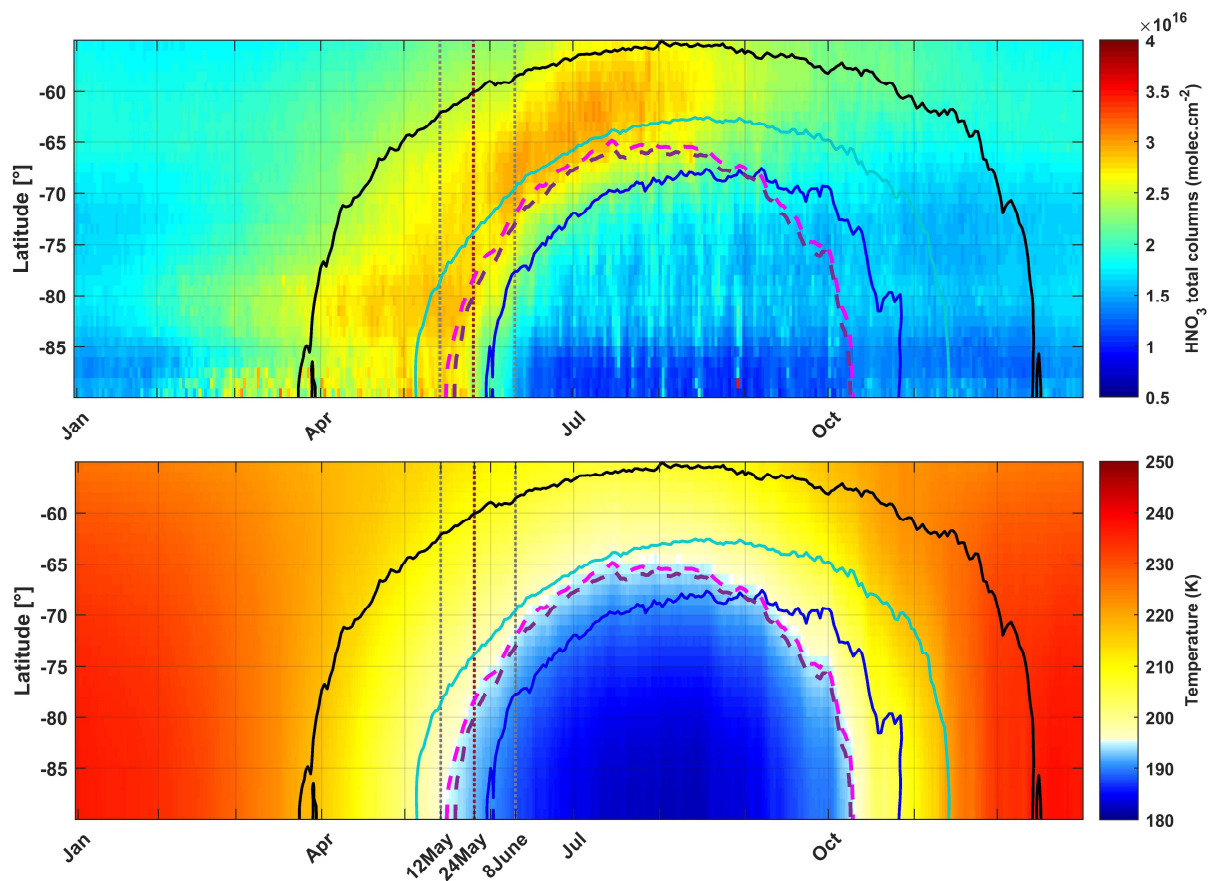
516  
 517  
 518  
 519  
 520  
 521  
 522  
 523  
 524  
 525  
 526  
 527  
 528  
 529  
 530  
 531  
 532  
 533

**Figure 3.** (a) Time series of daily averaged HNO<sub>3</sub> total columns (solid lines) and temperatures taken at 50 hPa (dashed lines) in the 70° - 90° S equivalent latitude band, for the years 2008 – 2017. The green dotted line represents the temperatures at 20 hPa for the year 2010. (b) HNO<sub>3</sub> total columns versus temperatures (at 50 hPa) histogram for the whole year (top) and for the 3 defined regimes (R1 - R3) separated in (a) for the year 2011. The colors refer to the number of gridded measurements in each cell. (c) Evolution of daily averaged HNO<sub>3</sub> total columns with the highest occurrence (in bins of 0.1×10<sup>16</sup> molec.cm<sup>-2</sup> and 2 K) as a function of the 50 hPa temperature for the years 2008 – 2017. The red horizontal or vertical lines represent the 195 K threshold temperature.

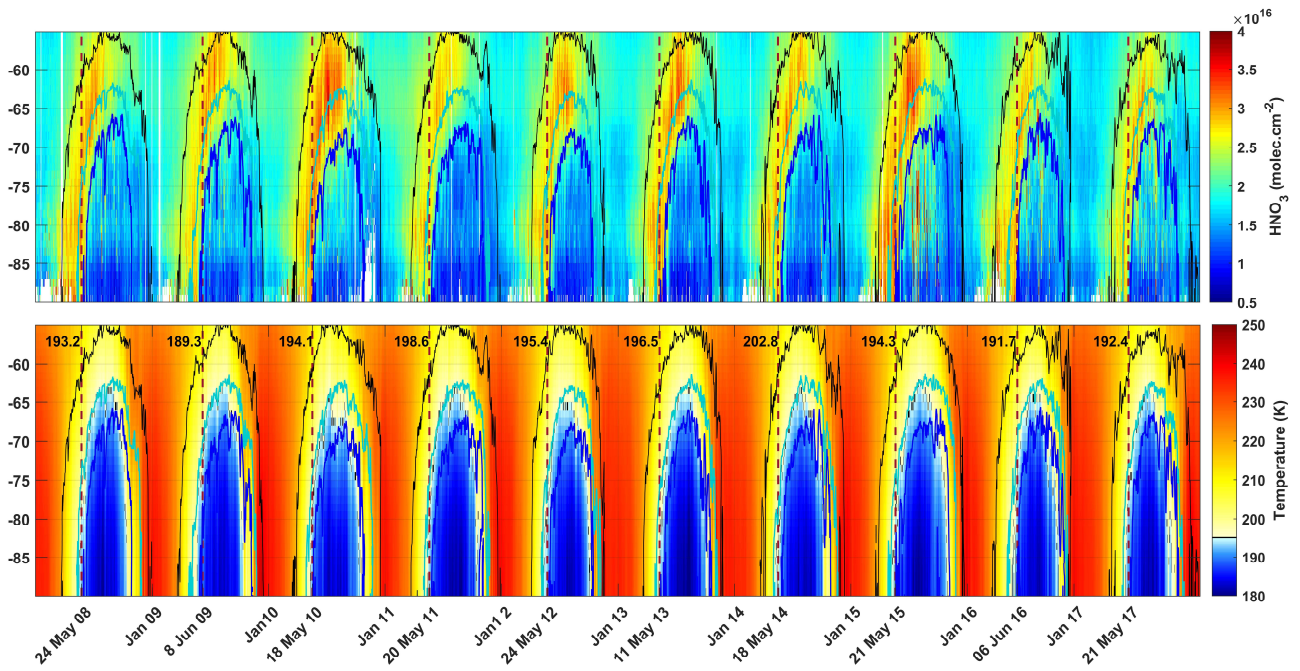


534  
 535  
 536  
 537  
 538  
 539  
 540  
 541  
 542  
 543  
 544  
 545

**Figure 4.** Time series of total HNO<sub>3</sub> second derivative (blue, left y-axis) and of the 50 hPa temperature (red, right y-axis), in the region of potential vorticity at 530 K lower than  $-10 \times 10^{-5} \text{ K} \cdot \text{m}^2 \cdot \text{kg}^{-1} \cdot \text{s}^{-1}$ . The red horizontal line corresponds to the 195 K temperature. The vertical dashed lines indicate the second derivative minimum in HNO<sub>3</sub> for each year. The corresponding dates (in bold, on the x-axis) and temperatures are also indicated. The time series of total HNO<sub>3</sub> second derivative (dashed blue) and of temperature (grey) in the 70° – 90° S Eqlat band are also represented.



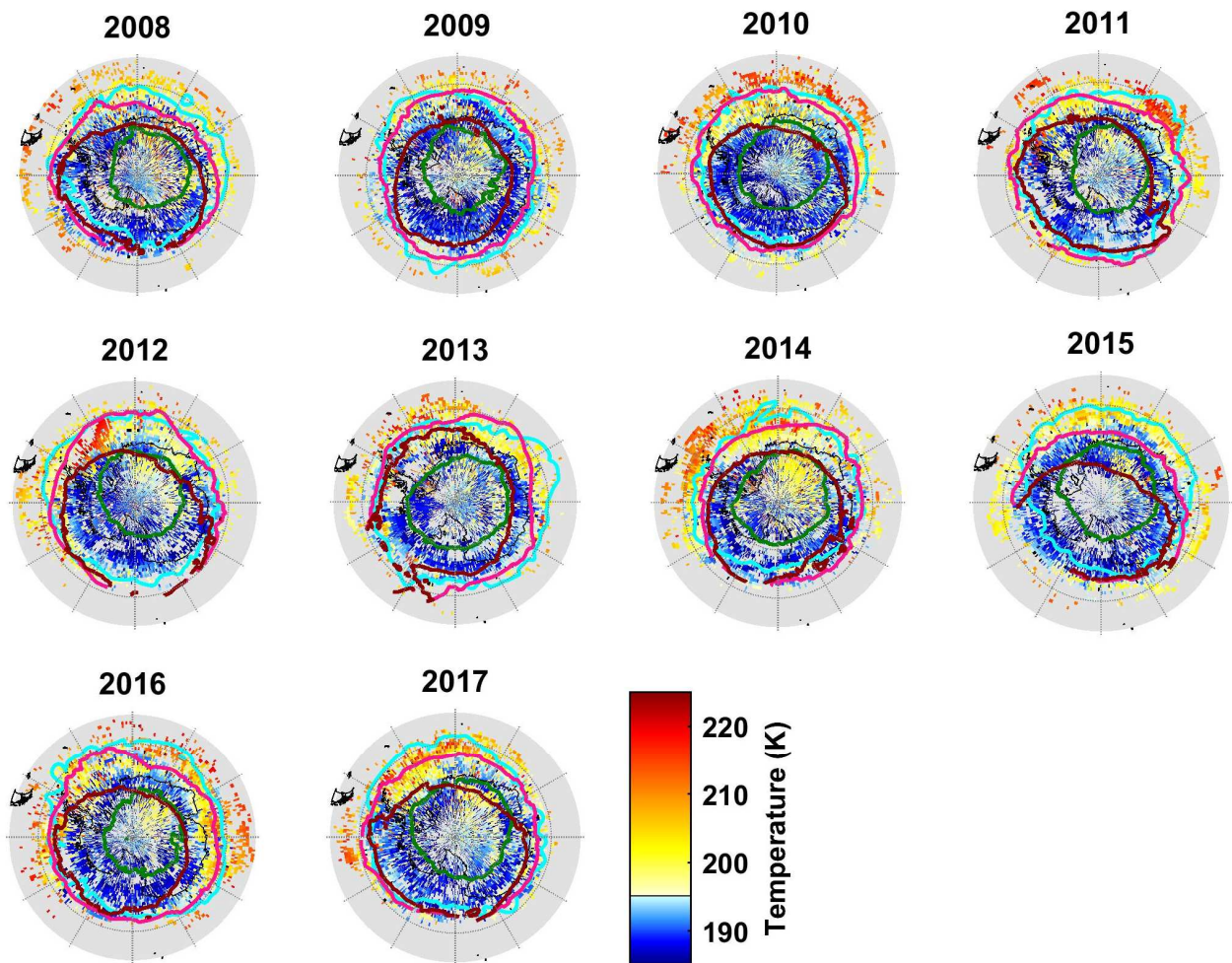
546  
 547 **Figure 5.** Zonal distributions of (a) HNO<sub>3</sub> total columns (in molec.cm<sup>-2</sup>) from IASI and (b) temperatures at 50  
 548 hPa from ERA Interim (in K) in the 55° S to 90° S geographical latitude band and averaged over the years 2008  
 549 – 2017. Three isocontours for PV of -5 (black), -8 (cyan) and -10 (blue) ( $\times 10^{-5}$  K.m<sup>2</sup>.kg<sup>-1</sup>.s<sup>-1</sup>) at 530 K, the  
 550 isocontours for the 195 K temperature (pink) and for the averaged 194.2 K drop temperature (purple) at 50 hPa  
 551 are superimposed. The vertical grey dashed lines mark the earliest and latest dates for the drop temperature  
 552 in the 10-year IASI record and the red one indicates the average date for the drop temperatures calculated in  
 553 the area delimited by a  $-10 \times 10^{-5}$  K.m<sup>2</sup>.kg<sup>-1</sup>.s<sup>-1</sup> PV contour.  
 554  
 555



556  
 557  
 558  
 559  
 560  
 561  
 562  
 563  
 564

**Figure 6.** Zonally averaged distributions of (top) HNO<sub>3</sub> total columns (in molec.cm<sup>-2</sup>) from IASI and (bottom) temperatures at 50 hPa from ERA Interim (in K). The geographical latitude range is from 55° to 90° south and the isocontours are PVs of -5 (black), -8 (cyan) and -10 (blue) ( $\times 10^{-5}$  K.m<sup>2</sup>.kg<sup>-1</sup>.s<sup>-1</sup> at 530 K). The vertical red dashed lines correspond to the second derivative minima each year in the area delimited by a  $-10 \times 10^{-5}$  K.m<sup>2</sup>.kg<sup>-1</sup>.s<sup>-1</sup> PV contour.





565  
566  
567  
568  
569  
570  
571  
572  
573  
574  
575  
576  
577  
578  
579  
580  
581  
582  
583

**Figure 7.** Spatial distribution ( $1^\circ \times 1^\circ$ ) of the drop temperature at 50 hPa (K) (calculated from the total  $\text{HNO}_3$  second derivative minima) for each year of IASI (2008–2017), in a region defined by a PV of  $-8 \times 10^{-5} \text{ K.m}^2.\text{kg}^{-1}.\text{s}^{-1}$ . The isocontours of  $-10 \times 10^{-5} \text{ K.m}^2.\text{kg}^{-1}.\text{s}^{-1}$  at 530 K for the averaged PV (in green) and the minimum PV (in cyan) encountered over the period 10 May –15 July for each year and the isocontours of 195 K at 50 hPa for the averaged (in red) and the minimum (in pink) temperatures over the same period are represented.

584  
585  
586  
587  
588  
589  
590  
591  
592  
593  
594  
595  
596  
597  
598  
599  
600  
601  
602  
603  
604  
605  
606  
607  
608  
609  
610  
611  
612  
613  
614  
615  
616  
617  
618  
619  
620  
621  
622  
623  
624  
625  
626  
627  
628  
629  
630  
631  
632  
633  
634  
635  
636  
637  
638  
639  
640  
641

## References

- Braun, M., Groöß, J.-U., Woiwode, W., Johansson, S., Höpfner, M., Friedl-Vallon, F., Oelhaf, H., Preusse, P., Ungermann, J., Sinnhuber, B.-M., Ziereis, H., and Braesicke, P.: Nitrification of the lowermost stratosphere during the exceptionally cold Arctic winter 2015/16, *Atmospheric Chemistry and Physics Discussions*, <https://doi.org/10.5194/acp-2019-108>, 2019.
- Carslaw, K. S., Luo, B. P., and Peter, T.: An analytical expression for the composition of aqueous {HNO<sub>3</sub>-H<sub>2</sub>SO<sub>4</sub>-H<sub>2</sub>O} stratospheric aerosols including gas phase removal of HNO<sub>3</sub>, *Geophys. Res. Lett.*, 22, 1877–1880, <https://doi.org/10.1029/95GL01668>, 1995.
- Carslaw, K. S., Wirth, M., Tsias, A., Luo, B. P., Dörnbrack, A., Leutbecher, M., Volkert, H., Renger, W., Bacmeister, J. T., Reimer, E., and Peter, T.: Increased stratospheric ozone depletion due to mountain-induced atmospheric waves, *Nature*, 391, 675–678, <https://doi.org/10.1038/35589>, 1998.
- Clerbaux, C., Boynard, A., Clarisse, L., George, M., Hadji-Lazaro, J., Herbin, H., Hurtmans, D., Pommier, M., Razavi, A., Turquety, S., Wespes, C., and Coheur, P.-F.: Monitoring of atmospheric composition using the thermal infrared IASI/MetOp sounder, *Atmospheric Chemistry and Physics*, 9, 6041–6054, <https://doi.org/10.5194/acp-9-6041-2009>, 2009.
- de Laat, A. T. J. and van Weele, M.: The 2010 Antarctic ozone hole: Observed reduction in ozone destruction by minor sudden stratospheric warmings, *Scientific Reports*, 1, 38, <https://doi.org/10.1038/srep00038>, 2011.
- de Zafra, R. and Smyshlyaev, S. P.: On the formation of HNO<sub>3</sub> in the Antarctic mid to upper stratosphere in winter, *Journal of Geophysical Research*, 106, 23 115, <https://doi.org/10.1029/2000JD000314>, 2001.
- Groöß, J. U., Engel, I., Borrmann, S., Frey, W., Günther, G., Hoyle, C. R., Kivi, R., Luo, B. P., Molleker, S., Peter, T., Pitts, M. C., Schlager, H., Stiller, G., Vömel, H., Walker, K. a., and Müller, R.: Nitric acid trihydrate nucleation and denitrification in the Arctic stratosphere, *Atmospheric Chemistry and Physics*, 14, 1055–1073, <https://doi.org/10.5194/acp-14-1055-2014>, 2014.
- Hanson, D. and Mauersberger, K.: Laboratory studies of the nitric acid trihydrate: Implications for the south polar stratosphere, *Geophysical Research Letters*, 15, 855–858, <https://doi.org/10.1029/GL015i008p00855>, 1988.
- Harris, N. R. P., Lehmann, R., Rex, M., and von der Gathen, P.: A closer look at Arctic ozone loss and polar stratospheric clouds, *Atmospheric Chemistry and Physics*, 10, 8499–8510, <https://doi.org/10.5194/acp-10-8499-2010>, 2010.
- Hilton, F., Armante, R., August, T., Barnet, C., Bouchard, A., Camy-Peyret, C., Capelle, V., Clarisse, L., Clerbaux, C., Coheur, P.-F., Collard, A., Crevoisier, C., Dufour, G., Edwards, D., Fajjan, F., Fourrié, N., Gambacorta, A., Goldberg, M., Guidard, V., Hurtmans, D., Illingworth, S., Jacquinet-Husson, N., Kerzenmacher, T., Klaes, D., Lavanant, L., Masiello, G., Matricardi, M., McNally, A., Newman, S., Pavelin, E., Payan, S., Péquignot, E., Peyridieu, S., Phulpin, T., Remedios, J., Schlüssel, P., Serio, C., Strow, L., Stubenrauch, C., Taylor, J., Tobin, D., Wolf, W., and Zhou, D.: Hyperspectral Earth Observation from IASI: Five Years of Accomplishments, *Bulletin of the American Meteorological Society*, 93, 347–370, <https://doi.org/10.1175/BAMS-D-11-00027.1>, 2012.
- Hoffmann, L., Spang, R., Orr, A., Alexander, M. J., Holt, L. A., and Stein, O.: A decadal satellite record of gravity wave activity in the lower stratosphere to study polar stratospheric cloud formation, *Atmospheric Chemistry and Physics*, 17, 2901–2920, <https://doi.org/10.5194/acp-17-2901-2017>, 2017.
- Höpfner, M., Luo, B. P., Massoli, P., Cairo, F., Spang, R., Snels, M., Di Donfrancesco, G., Stiller, G., von Clarmann, T., Fischer, H., and Biermann, U.: Spectroscopic evidence for NAT, STS, and ice in MIPAS infrared limb emission measurements of polar stratospheric clouds, *Atmospheric Chemistry and Physics*, 6, 1201–1219, <https://doi.org/10.5194/acp-6-1201-2006>, 2006.
- Höpfner, M., Pitts, M. C., and Poole, L. R.: Comparison between CALIPSO and MIPAS observations of polar stratospheric clouds, *Journal of Geophysical Research Atmospheres*, 114, 1–15, <https://doi.org/10.1029/2009JDO12114>, 2009.
- Hoyle, C. R., Engel, I., Luo, B. P., Pitts, M. C., Poole, L. R., Groöß, J. U., and Peter, T.: Heterogeneous formation of polar stratospheric clouds- Part 1: Nucleation of nitric acid trihydrate (NAT), *Atmospheric Chemistry and Physics*, 13, 9577–9595, <https://doi.org/10.5194/acp-13-9577-2013>, 2013.

642  
643 Hurtmans, D., Coheur, P.-F., Wespes, C., Clarisse, L., Scharf, O., Clerbaux, C., Hadji-Lazaro, J., George, M., and Turquety,  
644 S.: FORLI radiative transfer and retrieval code for IASI, *Journal of Quantitative Spectroscopy and Radiative Transfer*, 113,  
645 1391–1408, <https://doi.org/10.1016/j.jqsrt.2012.02.036>, 2012.

646  
647 James, A. D., Brooke, J. S. A., Mangan, T. P., Whale, T. F., Plane, J. M. C., and Murray, B. J.: Nucleation of nitric acid  
648 hydrates in polar stratospheric clouds by meteoric material, *Atmospheric Chemistry and Physics*, 18, 4519–4531,  
649 <https://doi.org/10.5194/acp-18-4519-2018>, 2018.

650  
651 Keys, J. G., Johnston, P. V., Blatherwick, R. D., and Murcray, F. J.: Evidence for heterogeneous reactions in the Antarctic  
652 autumn stratosphere, *Nature*, 361, 49–51, <https://doi.org/10.1038/361049a0>, 1993.

653  
654 Klekociuk, A., Tully, M., Alexander, S., Dargaville, R., Deschamps, L., Fraser, P., Gies, H., Henderson, S., Javorniczky, J.,  
655 Krummel, P., Petelina, S., Shanklin, J., Siddaway, J., and Stone, K.: The Antarctic ozone hole during 2010, *Australian  
656 Meteorological and Oceanographic Journal*, 61, 253–267, <https://doi.org/10.22499/2.6104.006>, 2011.

657  
658 Koop, T., Luo, B., Tsias, A., and Peter, T.: Water activity as the determinant for homogeneous ice nucleation in aqueous  
659 solutions, *Nature*, 406, 611–614, <https://doi.org/10.1038/35020537>, 2000.

660  
661 Lambert, A. and Santee, M. L.: Accuracy and precision of polar lower stratospheric temperatures from reanalyses evaluated  
662 from A-Train CALIOP and MLS, COSMIC GPS RO, and the equilibrium thermodynamics of supercooled ternary solutions  
663 and ice clouds, *Atmospheric Chemistry and Physics*, 18, 1945–1975, <https://doi.org/10.5194/acp-18-1945-2018>, 2018.

664  
665 Lambert, A., Santee, M. L., Wu, D. L., and Chae, J. H.: A-train CALIOP and MLS observations of early winter Antarctic  
666 polar stratospheric clouds and nitric acid in 2008, *Atmospheric Chemistry and Physics*, 12, 2899–2931,  
667 <https://doi.org/10.5194/acp-12-2899-2012>, 2012.

668  
669 Lambert, A., Santee, M. L., and Livesey, N. J.: Interannual variations of early winter Antarctic polar stratospheric cloud  
670 formation and nitric acid observed by CALIOP and MLS, *Atmospheric Chemistry and Physics*, 16, 15 219–15 246,  
671 <https://doi.org/10.5194/acp-16-15219-2016>, 2016.

672  
673 Lowe, D. and MacKenzie, A. R.: Polar stratospheric cloud microphysics and chemistry, *Journal of Atmospheric and Solar-  
674 Terrestrial Physics*, 70, 13–40, <https://doi.org/10.1016/j.jastp.2007.09.011>, 2008.

675  
676 Molleker, S., Borrmann, S., Schlager, H., Luo, B., Frey, W., Klingebiel, M., Weigel, R., Ebert, M., Mitev, V., Matthey, R.,  
677 Woiwode, W., Oelhaf, H., Dörnbrack, A., Stratmann, G., Groß, J.-U., Günther, G., Vogel, B., Müller, R., Krämer, M.,  
678 Meyer, J., and Cairo, F.: Microphysical properties of synoptic-scale polar stratospheric clouds: in situ measurements of  
679 unexpectedly large HNO<sub>3</sub>-containing particles in the Arctic vortex, *Atmospheric Chemistry and Physics*, 14, 10 785–10 801,  
680 <https://doi.org/10.5194/acp-14-10785-2014>, 2014.

681  
682 Murphy, D. M. and Koop, T.: Review of the vapour pressures of ice and supercooled water for atmospheric applications,  
683 *Quarterly Journal of the Royal Meteorological Society*, 131, 1539–1565, <https://doi.org/10.1256/qj.04.94>, 2005.

684  
685 Peter, T.: Microphysics and heterogeneous chemistry of polar stratospheric clouds, *Annual Review of Physical Chemistry*,  
686 48, 785–822, <https://doi.org/10.1146/annurev.physchem.48.1.785>, 1997.

687  
688 Peter, T. and Groß, J.-U.: Chapter 4. Polar Stratospheric Clouds and Sulfate Aerosol Particles: Microphysics, Denitrification  
689 and Heterogeneous Chemistry, in: *Stratospheric Ozone Depletion and Climate Change*, pp. 108–144, Royal Society of  
690 Chemistry, <https://doi.org/10.1039/9781849733182-00108>, 2012.

691  
692 Piccolo, C. and Dudhia, A.: Precision validation of MIPAS-Envisat products, *Atmospheric Chemistry and Physics*, 7, 1915–  
693 1923, <https://doi.org/10.5194/acp-7-1915-2007>, 2007.

694  
695 Pitts, M. C., Poole, L. R., Dörnbrack, A., and Thomason, L. W.: The 2009–2010 Arctic polar stratospheric cloud season: A  
696 CALIPSO perspective, *Atmospheric Chemistry and Physics*, 11, 2161–2177, <https://doi.org/10.5194/acp-11-2161-2011>,  
697 2011.

698

699 Pitts, M. C., Poole, L. R., Lambert, A., and Thomason, L.W.: An assessment of CALIOP polar stratospheric cloud  
700 composition classification, *Atmospheric Chemistry and Physics*, 13, 2975–2988, <https://doi.org/10.5194/acp-13-2975-2013>,  
701 2013.

702  
703 Pitts, M. C., Poole, L. R., and Gonzalez, R.: Polar stratospheric cloud climatology based on CALIPSO spaceborne lidar  
704 measurements from 2006 to 2017, *Atmospheric Chemistry and Physics*, 18, 10 881–10 913, <https://doi.org/10.5194/acp-18-10881-2018>, 2018.

705  
706  
707 Rodgers, C. D.: *Inverse Methods for Atmospheric Sounding - Theory and Practice*, vol. 2 of Series on Atmospheric Oceanic  
708 and Planetary Physics, World Scientific Publishing Co. Pte. Ltd., <https://doi.org/10.1142/9789812813718>, 2000.

709  
710 Ronsmans, G., Langerock, B., Wespes, C., Hannigan, J. W., Hase, F., Kerzenmacher, T., Mahieu, E., Schneider, M., Smale,  
711 D., Hurtmans, D., De Mazière, M., Clerbaux, C., and Coheur, P.-F.: First characterization and validation of FORLI-HNO<sub>3</sub>  
712 vertical profiles retrieved from IASI/Metop, *Atmospheric Measurement Techniques*, 9, 4783–4801,  
713 <https://doi.org/10.5194/amt-9-4783-2016>, 2016.

714  
715 Ronsmans, G., Wespes, C., Hurtmans, D., Clerbaux, C., and Coheur, P.-F.: Spatio-temporal variations of nitric acid total  
716 columns from 9 years of IASI measurements – a driver study, *Atmospheric Chemistry and Physics*, 18, 4403–4423,  
717 <https://doi.org/10.5194/acp-18-4403-2018>, 2018.

718  
719 Santee, M. L., Manney, G. L., Froidevaux, L., Read, W. G., and Waters, J. W.: Six years of UARS Microwave Limb Sounder  
720 HNO<sub>3</sub> observations : Seasonal, interhemispheric, and interannual variations in the lower stratosphere, *Journal of Geophysical*  
721 *Research*, 104, 8225–8246, <https://doi.org/10.1029/1998JD100089>, 1999.

722  
723 Santee, M. L., Lambert, A., Read, W. G., Livesey, N. J., Cofield, R. E., Cuddy, D. T., Daffer, W. H., Drouin, B. J., Froidevaux,  
724 L., Fuller, R. A., Jarnot, R. F., Knosp, B. W., Manney, G. L., Perun, V. S., Snyder, W. V., Stek, P. C., Thurstans, R. P.,  
725 Wagner, P. A., Waters, J. W., Muscari, G., de Zafra, R. L., Dibb, J. E., Fahey, D. W., Popp, P. J., Marcy, T. P., Jucks, K. W.,  
726 Toon, G. C., Stachnik, R. A., Bernath, P. F., Boone, C. D., Walker, K. A., Urban, J., and Murtagh, D.: Validation of the Aura  
727 Microwave Limb Sounder HNO<sub>3</sub> measurements, *Journal of Geophysical Research*, 112, 1–22,  
728 <https://doi.org/10.1029/2007JD008721>, 2007.

729  
730 Schreiner, J., Voigt, C., Weisser, C., Kohlmann, A., Mauersberger, K., Deshler, T., Kröger, C., Rosen, J., Kjome, N., Larsen,  
731 N., Adriani, A., Cairo, F., Donfrancesco, G. D., Ovarlez, J., Ovarlez, H., and Dörnbrack, A.: Chemical , microphysical , and  
732 optical properties of polar stratospheric clouds, *Journal of Geophysical Research*, 108, 1–10,  
733 <https://doi.org/10.1029/2001JD000825>, 2003.

734  
735 Sheese, P. E., Walker, K. A., Boone, C. D., Bernath, P. F., Froidevaux, L., Funke, B., Raspollini, P., and von Clarmann, T.:  
736 ACE-FTS ozone, water vapour, nitrous oxide, nitric acid, and carbon monoxide profile comparisons with MIPAS and MLS,  
737 *Journal of Quantitative Spectroscopy and Radiative Transfer*, 186, 63–80, <https://doi.org/10.1016/j.jqsrt.2016.06.026>, 2017.

738  
739 Snels, M., Scoccione, A., Liberto, L. D., Colao, F., Pitts, M., Poole, L., Deshler, T., Cairo, F., Cagnazzo, C., and Fierli, F.:  
740 Comparison of Antarctic polar stratospheric cloud observations by ground-based and space-borne lidar and relevance for  
741 chemistry–climate models, *Atmospheric Chemistry and Physics*, 19, 955–972, <https://doi.org/10.5194/acp-19-955-2019>,  
742 2019.

743  
744 Solomon, S.: Stratospheric ozone depletion: A review of concepts and history, *Reviews of Geophysics*, 37, 275–316,  
745 <https://doi.org/10.1029/1999RG900008>, 1999.

746  
747 Spang, R., Hoffmann, L., Höpfner, M., Griessbach, S., Müller, R., Pitts, M. C., Orr, A. M. W., and Riese, M.: A multi-  
748 wavelength classification method for polar stratospheric cloud types using infrared limb spectra, *Atmospheric Measurement*  
749 *Techniques*, 9, 3619–3639, <https://doi.org/10.5194/amt-9-3619-2016>, 2016.

750  
751 Spang, R., Hoffmann, L., Müller, R., Groß, J.-U., Tritscher, I., Höpfner, M., Pitts, M., Orr, A., and Riese, M.: A climatology  
752 of polar stratospheric cloud composition between 2002 and 2012 based on MIPAS/Envisat observations, *Atmospheric*  
753 *Chemistry and Physics*, 18, 5089–5113, <https://doi.org/10.5194/acp-18-5089-2018>, 2018.

754  
755 Toon, O. B., Hamill, P., Turco, R. P., and Pinto, J.: Condensation of HNO<sub>3</sub> and HCl in the winter polar stratospheres,  
756 *Geophysical Research Letters*, 13, 1284–1287, <https://doi.org/10.1029/GL013i012p01284>, 1986.

757  
758 Tritscher, I., Pitts, M. C., Poole, L. R., Alexander, S. P., Cairo, F., Chipperfield, M. P., et al.: Polar stratospheric clouds:  
759 Satellite observations, processes, and role in ozone depletion, *Reviews of Geophysics*, 59, e2020RG000702,  
760 <https://doi.org/10.1029/2020RG000702>.  
761  
762 Urban, J., Pommier, M., Murtagh, D. P., Santee, M. L., and Orsolini, Y. J.: Nitric acid in the stratosphere based on Odin  
763 observations from 2001 to 2009 – Part 1: A global climatology, *Atmospheric Chemistry and Physics*, 9, 7031–7044,  
764 <https://doi.org/10.5194/acp-9-7031-2009>, 2009.  
765  
766 Voigt, C., Schreiner, J., Kohlmann, A., Zink, P., Mauersberger, K., Larsen, N., Deshler, T., Kro, C., Rosen, J., Adriani, A.,  
767 Cairo, F., Donfrancesco, G. D., Viterbini, M., Ovarlez, J., Ovarlez, H., and David, C.: Nitric Acid Trihydrate (NAT) in Polar  
768 Stratospheric Clouds, *Science*, 290, 1756–1758, <https://doi.org/10.1126/science.290.5497.1756>, 2000.  
769  
770 Voigt, C., Larsen, N., Deshler, T., et al.: In situ mountainwave polar stratospheric cloud measurements: Implications for nitric  
771 acid trihydrate formation, *J. Geophys. Res.*, 108(D5), doi:10.1029/2001JD001185, 2003.  
772  
773 Voigt, C., Schlager, H., Luo, B. P., Dörnbrack, A., Roiger, A., Stock, P., Curtius, J., Vössing, H., Borrmann, S., Davies, S.,  
774 Konopka, P., Schiller, C., Shur, G., and Peter, T.: Nitric Acid Trihydrate (NAT) formation at low NAT supersaturation in  
775 Polar Stratospheric Clouds (PSCs), *Atmospheric Chemistry and Physics*, 5, 1371–1380, [https://doi.org/10.5194/acp-5-1371-](https://doi.org/10.5194/acp-5-1371-2005)  
776 2005, 2005.  
777  
778 von König, M.: Using gas-phase nitric acid as an indicator of PSC composition, *Journal of Geophysical Research*, 107,  
779 <https://doi.org/10.1029/2001jd001041>, 2002.  
780  
781 Wang, X. and Michelangeli, D. V.: A review of polar stratospheric cloud formation, *China Particuology*, 4, 261–271,  
782 [https://doi.org/10.1016/S1672-2515\(07\)60275-9](https://doi.org/10.1016/S1672-2515(07)60275-9), 2006.  
783  
784 Wegner, T., Groß, J.-U., von Hobe, M., Stroh, F., Sumin´ska-Ebersoldt, O., Volk, C. M., Hösen, E., Mitev, V., Shur, G.,  
785 and Müller, R.: Heterogeneous chlorine activation on stratospheric aerosols and clouds in the Arctic polar vortex,  
786 *Atmospheric Chemistry and Physics*, 12, 11 095–11 106, <https://doi.org/10.5194/acp-12-11095-2012>, 2012.  
787  
788 Wespes, C., Hurtmans, D., Clerbaux, C., and Coheur, P.-F.: O<sub>3</sub> variability in the troposphere as observed by IASI over 2008-  
789 2016: Contribution of atmospheric chemistry and dynamics, *Journal of Geophysical Research: Atmospheres*, 122, 2429–  
790 2451, <https://doi.org/10.1002/2016JD025875>, <http://doi.wiley.com/10.1002/2016JD025875>, 2017.  
791  
792 WMO: Scientific Assessment of Ozone Depletion: 2014, Global Ozone Research and Monitoring Project – Report No. 55,  
793 World Meteorological Organization, Geneva, Switzerland, 2014.  
794  
795 Zhu, Y., Toon, O. B., Lambert, A., Kinnison, D. E., Brakebusch, M., Bardeen, C. G., Mills, M. J., and English, J. M.:  
796 Development of a Polar Stratospheric Cloud Model within the Community Earth System Model using constraints on Type I  
797 PSCs from the 2010-2011 Arctic winter, *Journal of Advances in Modeling Earth Systems*, 7, 551–585,  
798 <https://doi.org/10.1002/2015ms000427>, 2015.  
799  
800 Zondlo, M. A., P. K. Hudson, A. J. Prenni, and M. A. Tolbert: Chemistry and microphysics of polar stratospheric clouds and  
801 cirrus clouds, *Annu. Rev. Phys. Chem.*, 51, 473–499, 2000.